FEM BASED DESIGN OF EXPERIMENT FOR TRAIN WHEELSET DIAGNOSTICS BY LASER ULTRASONICS

A. Cavuto[a*], M. Martarelli[a], G. Pandarese[a], G.M. Revel[a], E.P. Tomasini[a]

a. Università Politecnica delle Marche, Via Brecce Bianche, Ancona

Corresponding author: g.pandarese@univpm.it

DIISM, Università Politecnica delle Marche, Ancona, Italy

Abstract.

Laser-Ultrasonics Testing (LUT) is a Non-Destructive Technique (NDT) with good potential for application in the railway sector, nevertheless this technique is not yet used in practice because there are some practical difficulties to overcome. The possibility of measuring on a complete wheelset by bypassing the keying of the wheel will allow drastically reducing the inspection time but it has not yet been demonstrated. In fact, the attenuation of the signal in the path makes complex the interpretation of the generated waves. This paper aims at illustrating how the combination of simulated and experimental data allows to optimize the test setup for having output data of unambiguous interpretation. The main innovations presented in this paper are: (i) the possibility to work with low energy waves in the thermoelastic-ablative limit while maintaining satisfactory contrast levels for the purpose of defect detection and (ii) the implementation of a complete Finite Element Model (FEM) including the generation and propagation of waves in the solid domain and the propagation in air. This last step has not considered before in previous papers. The model allows to define the optimal experimental conditions to have a measured signal with an adequate signal-to-noise ratio (SNR> 6 dB) and to define an experimental procedure for defect detection reliable and comparable with current standards. This study lays the foundations for an innovative approach for train axle diagnostics which can be used during train extraordinary maintenance interventions. The laser ultrasonics system presented in this paper can be likely integrated in the pit lathe and exploited to monitor the railway wheels during their re-profiling phase, without having to remove them from the vehicle.

Keywords: Laser-ultrasonics, NDT, air-coupled ultrasound, train wheelset, FE modelling

1. Introduction

The development of Non-Destructive Testing (NDT) procedures is a topic of great impact, especially in the train sector, whose aim is the early identification of cracks whose propagation can cause faults and accidents. Those procedures are commonly applied for the identification of damages and defects on train wheelset during extraordinary maintenance. Defects can occur on the wheels because they are exposed to high loads caused by wheel-rail contact, leading to the generation and propagation of defects. Axles are constantly exposed to cyclic rotating bending superposed with torsion, occurring during regular maneuvers like cornering of trains or deceleration and acceleration. These mixed-mode loading conditions cause fatigue processes inducing crack nucleation and propagation, as studied in [1]. Furthermore, axle bending and vibration induce common fatigue cracks along geometrical transitions (like the axle fillet radii) and repetitive micro sliding between wheel and axle itself on the press-fit seat also called fretting fatigue, as described in [2] and [3]. That mechanism is one of the main sources of crack nucleation in the wheel-axle press-fit that is an inaccessible region for inspection unless the wheelset is disassembled.

The procedures based on non-destructive tests are constantly evolving to meet the European standards EN 15313, [4], and the directives of the National Agency for Safety of Railways (ANSF), guiding the regulation on the safety of railway traffic.

The current standard methods for the detection of radial defects are based on ultrasound phased array. An automated procedure for the inspection of hollow axles has been presented in [5]; a semi-automated rotating probe mounting differently angled transducers has been described in [6] with its application to solid axles. The exploitation of phased array techniques for wheel tread damage detection has been illustrated in [7]. Automated systems equipped with phased arrays tailored for the specific application are available in the market even though they are currently unattractive, given the high costs associated to the acquisition of instrumentation and the adaptation of test benches to these systems. The main disadvantages of phased arrays are the difficulty on the adaptation to different wheel profiles and the complexity of the measurement set-up, e.g. of the system for the accumulation, injection and recovery of the coupling mean, necessary in the application of contact probes.

Air-coupled ultrasound probes can solve the above-mentioned problems, but, while their application as receiving transducers is feasible, the use of non-contact ultrasound exciters is almost prohibitive.

In fact, the high difference of impedance between air and solid will cause more than 99% of the incident wave to be reflected into the air.

Laser-Ultrasonics Testing (LUT) systems instead are non-contact techniques, based on high power laser sources exploited as ultrasonic waves exciters. Some LUT configurations [8], [9] make use of laser interferometers as receiving probes to detect the elastic waves propagating into the solid material. Notwithstanding, the application of laser interferometers is highly influenced by the surface condition of the object under test. The measurement surface must be diffusive, but this is not the case with axles under test during maintenance operations. Their surface is often dirty, i.e. covered with dust, oil or grease and those substances absorb laser light. On the other way around, if the axle is clean the steel surface is highly reflective and the setting of a correct laser angular position is crucial, especially for curved surfaces, for having a good backscattering of the laser light into the receiving photodiode. For that reason, the best compromise is to use a LUT configuration based on high power lasers for ultrasound generation and air-coupled receiving probes, exhibiting flexibility in installation and operation.

At present LUT methods have been only applied to disassembled wheelset, i.e. to dismounted axles, like in [10] and [8], and wheels, as presented in [9], [11], [12]. This is due to the fact that the energy of the ultrasound waves is strongly attenuated when travelling through discontinuities like the wheel-axle press-fit region. Additionally, discontinuities produce scattering of ultrasound waves that generates false positives or buries the scattering induced by real defects located in the axle fillet radii regions in which there is the greatest probability of presence of defects caused by common fatigue.

In this paper, the authors have demonstrated the applicability of a LUT method for the detection of cracks located in the geometric transition regions close to the wheel seats on a complete wheelset. Experimental data have been presented by the same authors in [13]. In that work it has been evidenced how it is difficult to measure in those prohibitive regions where the ultrasound waves propagation is extremely complex. In this paper a method making use of the inputs derived from a numerical FE model is presented. Specifically, the modeled ultrasound propagation on the tested object allowed to identify the optimal working conditions to achieve an adequate contrast between sound and damaged regions and make the procedure for fault detection reliable and comparable with current standards.

The FE model has been developed to simulate the mechanisms that governs the generation of elastic waves in solids in both the thermos-elastic and ablative regimes, the interaction of the laser wave with the material it impacts on, the propagation of ultrasound waves in the material and their interaction with typical defects. This kind of models have been applied in the railway sector and in particular for the simulation of ultrasound waves propagation in axles, as presented in [10], in wheels [12] and wheelset sections [14]. The latter is the most complete model because it considers the whole wheelset, but it is limited to the simulation of the elastic waves' propagation within the solid material. It is therefore very useful for the simulation of ultrasound waves received by contact probes but no enforceable for air-coupled ultrasonic inspections. In this paper, the FE model has been exploited to replicate a non-contact laser-ultrasonics experiment, where the receiving probe is air-coupled and therefore the propagation of the elastic waves in the air domain between the axle surface and the receiving probe has been considered in the simulation. This is one of the main innovations of the paper, since the numerical models presented in the state of the art considered only the generation and propagation of waves in the solid domain and neglected the propagation in air.

Finally, the FE model developed has been exploited as a Design of Experiment instrument that allows to identify the optimal experimental parameters. This made it possible to limit the ultrasound wave energy in the thermoelastic-ablative limit while maintaining satisfactory contrast levels for the purpose of defect detection and making the procedure for the detection of defects reliable and comparable with current standards.

2. Laser-Ultrasonics test numerical simulation

To evaluate the efficiency of the air-coupled laser-ultrasonics technique in terms of its ability to detect defects in the wheelset, a numerical model for the design of experiment (DOE) was developed in order to:

- identify the optimal position of the air coupled transducer in terms of its angular orientation along the lateral surface of the train axle;
- determine the elastic wave propagation within the axle material and in the air between the axle surface and the receiving probe in order to recognize which type of propagation mode (longitudinal, shear, surface) is more sensitive to the presence of a defect;
- define the time window to analyze within the time history acquired depending on the propagation mode to be selected, in relation to the previous point.

The model must simulate a typical LUT experiment applied to a wheelset, see Fig. 1(a), with the ultrasonic excitation and receiving probe located at different sides of the wheel and working in transmission mode. This configuration has several advantages with respect to a standard configuration where the exciter and receiver are side-by-side at the same side of the wheel and work in reflection mode. First, the configuration in transmission mode is a sort of blind experiment that works with any defect position regardless its location in the propagation path. In addition, when working in reflection mode, the waves reflected by the section variation could be greater than the wave reflected by the defect, making them difficult to be sensitive to the defect occurrence. By working in transmission mode, the reflected waves will be systematically excluded. Finally, the laser impact on the surface in the presence of oil or grease will generate a detonation of dirt particles that can damage the ultrasound transducer, when positioned next to the exciter. Additionally, the laser impact onto the solid material will induce a strong reflection into the surrounding air, which causes a saturation of the receiving piezoelectric transducer thus degrading the received ultrasonic signal. The numerical model will be exploited to simulate the propagation of the ultrasonic waves generated by a high-power laser source and travelling within the axle material, passing through the axle-wheel interface and propagating through the air before reaching the receiving probe. The propagation path is illustrated in Fig. 1(b). The Rayleigh wave undergoes a strong attenuation along the path that goes from the laser source to the non-contact receiving probe. In fact, part of the attenuation occurs when the Rayleigh wave passes through the various filling regions and the wheel fitting seat on the axle, the so-called fretting region (see Fig. 1(a)).

The wheel is fitted on the axle with a force fit that has negative allowance [15]; the wheel hub being smaller than the axle means that the contact pressure ensures the transfer of the load between the two. As described in [14], it can be expected that a fraction of the Rayleigh wave will be converted from surface to bulk modes, but a fraction of it will propagate along the interface between the axle and the wheel. In the propagation path, the Rayleigh wave will experience, then, a strong attenuation that will be increased when the propagation passes from solid to air to reach the non-contact receiving probe. In fact, in the solid-air transition zone, the propagation of the Rayleigh wave leads to the generation of longitudinal bulk waves (see Fig. 1(b)) in the air whose energy contents are very low due to the high difference in acoustic impedance between the two media (steel and air).

For this reason, the development of a validated FE model able to simulate the propagation of high-frequency ultrasonic waves both in the wheelset section and air domain makes it possible to have an effective tool to guide the design of the experimental procedure based on non-contact LUT aiming at maximizing the SNR of the output signal from the non-contact receiving transducer while minimising the laser pulse energy below the threshold of surface damage.

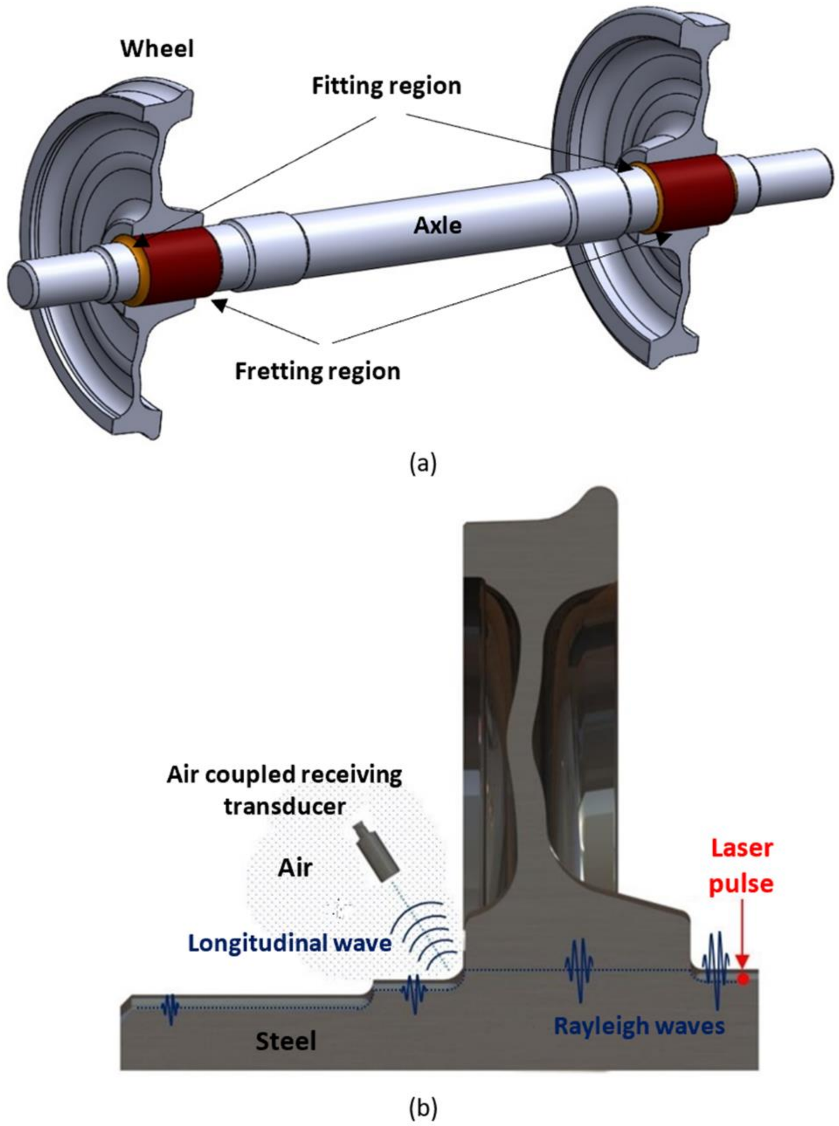

Fig. 1. Wheelset geometry (a) and visualisation of the propagation of the elastic waves (b).

2.1. Numerical FE model

COMSOL Multiphysics software was used to carry out the numerical simulation. The FE model developed was validated both on a simplified test item [16] and on a portion of a train axle [10].

Two physics, thermal stress and acoustic-structure interaction were exploited to simulate the generation and propagation of elastic waves both in the wheelset section and the air gap between the axle surface and the receiving probe.

The generation of the elastic waves in the laser incident location was modelled following the thermal diffusion and thermo-elastic displacement equations [17]:

The absorption of the laser pulse on the surface of the axle was assumed to occur without phase change, considering a thermo-elastic model with a heat flux of 16.9 MW/cm^2 that is lower than the limit between the thermo-elastic and the ablative regimes of generation [18].

The steel physical parameters used in the equations implemented in the numerical model are presented in the Table 1.

Table 1 Physical parameters of steel used in the model.

ρ	Density	7900 kg/m^3
E	Young Modulus (@ 273.15 K)	200 GPa
C	Specific heat capacity	480 J/(kg K)
υ	Poisson’s ratio	0.291
k	Thermal conductivity	50 W/(m K)
α	Coefficient of thermal expansion	10.7 e-6 K-1
R	Reflection coefficient	0.3
Ac	Absorption coefficient	3.87 e9 m-1

The propagation of the elastic wave within the wheelset was modelled with the wave equation obtained from Newton’s second law while the propagation in the air domain was modelled with the wave equation identifying the pressure distribution [19].

The boundary condition between the train axle and the wheel domains was set as contact condition to model the fittings between wheel and axle. The contact has been simulated by using contact pair nodes. The augmented Lagrangian algorithm was applied to compute the contact in the normal direction. The contact in the tangential direction has been simulated by using the classical Coulomb approach considering a static frictional coefficient μ_{stat} with a value of 0.6 [15]. Automatic contact controls were adopted to improve the convergence. For a reliable simulation of surface wave propagation, the wheel was considered to be mounted on the axle with suitable contact pressures in accordance with UIC 813 and the EN 13260 standards.

Fig. 2 shows the modelled geometry and domains in relation to the real wheelset; the boundary conditions are also reported. The boundaries corresponding to the model truncation have been set as low-reflecting boundary and sound soft boundary in the case of solid and air domain, respectively, to avoid reflections.

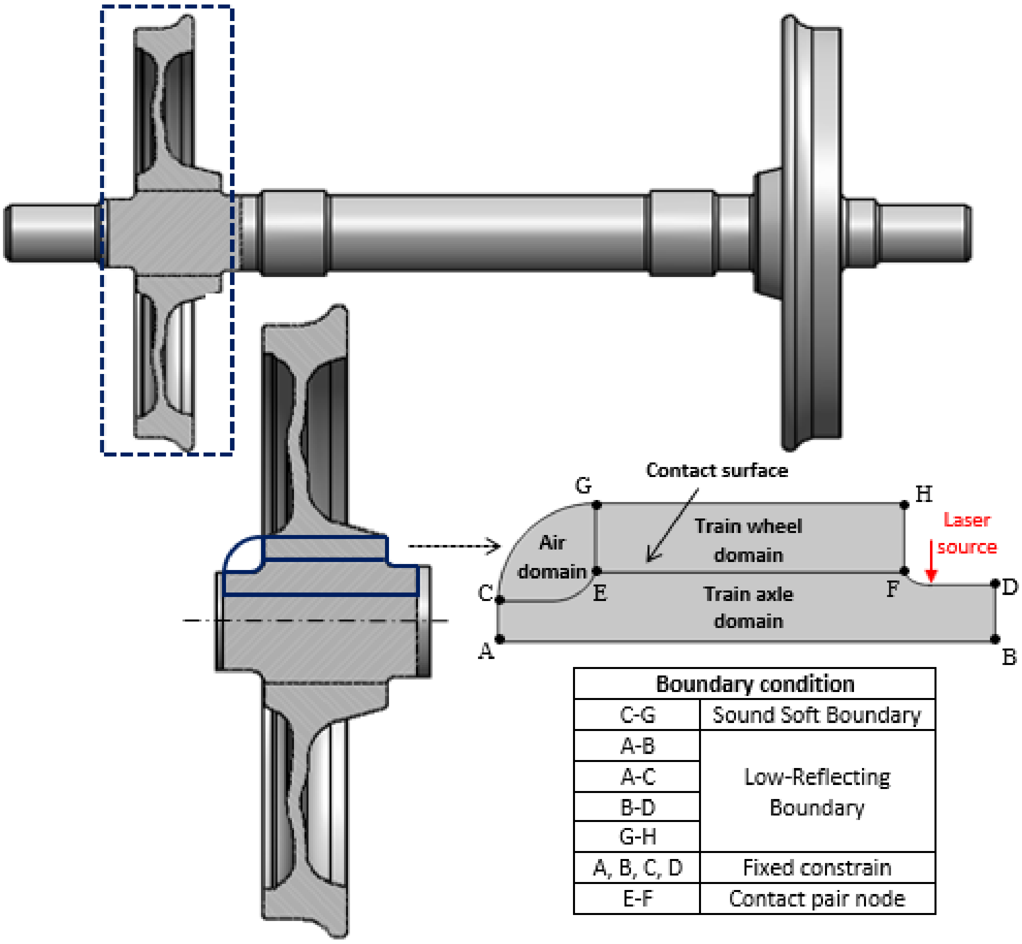

Fig. 2. 2D numerical model of the axle and wheel.

Key parameters for the convergence of the numerical algorithm and for the simulation accuracy are the time and spatial resolution. Concerning the time resolution or integration time step it has been established in [19] that it can be calculated using the following expression:

$$\Delta t = \frac{1}{180 f_{max}} \quad (1)$$

where f_{max} is the highest frequency of interest, 500 kHz in our case. The selection of f_{max} is related to the frequency content of ultrasonic wave generated by the laser and propagating into the solid material and in the air and to the sensitivity of air coupled ultrasonic probes. In order to determine the frequency content of the ultrasonic wave in the proximity of the generation area, a measurement of the axle surface displacement has been performed by means of a laser Doppler interferometer (Polytec OFV5000- DD300) with a frequency bandwidth of 20 MHz. The measurement position was set in an undamaged region at a distance of 37 mm from the laser source, which is the minimum distance to avoid interference of the laser source to the receiving one [20]. The frequency spectrum of the surface displacement is shown in Fig. 3 and it evidences that the ultrasound wave frequency content is limited below 2 MHz.

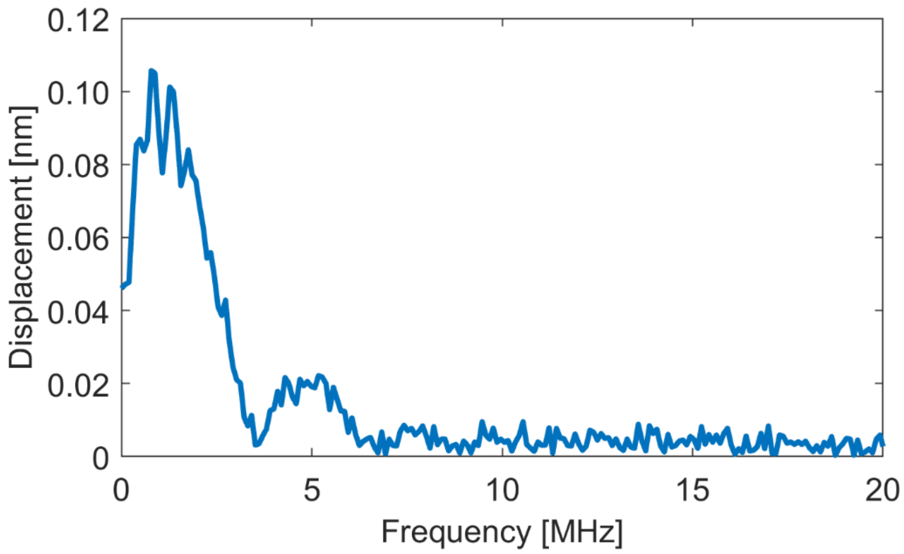

Fig. 3. Frequency spectrum of the axle surface displacement related to the ultrasound wave propagation into the material.

The second driver for the selection of the operating frequency of the ultrasound probe employed is its sensitivity, which is inversely proportional to the frequency for air-coupled transducers [21]. As an example, for Ultran Group 500 kHz (NCG500-D19) and 1 MHz (NCT1-D13) probes the sensitivity is -50 dB and – 56 dB respectively. Since the scope of this work is to demonstrate the applicability of the measurement technique at large distances from the laser source, where the SNR is extremely limited, a probe with 500 kHz operating frequency was selected. To demonstrate that the 1 MHz probe has lower sensitivity with respect to the 500 kHz one, the frequency spectra of the signals acquired with the two probes beyond the wheel on the same position on the axle in an undamaged region are reported in Fig. 4.

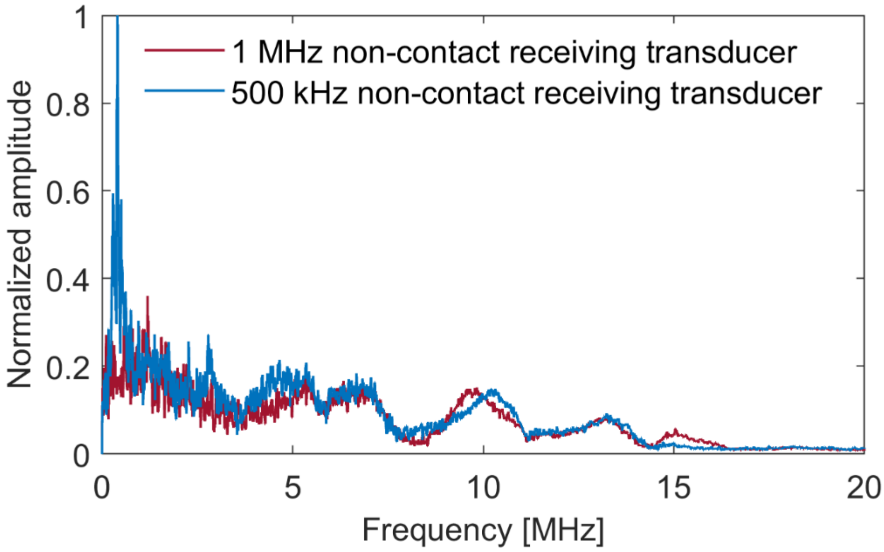

Fig. 4. Frequency spectra of the ultrasonic wave acquired by air-coupled ultrasound probes: Ultran Group NCG500-D19, 500 kHz probe and NCT1-D13, 1 MHz probe.

The time resolution was also related to laser pulse duration which was of the order of nanoseconds (≈12 ns), because the time step must be suitable to accurately sample the laser pulse time history.

The simulations were therefore carried out with an integration time step of 3 ns. Concerning the spatial resolution, it depends to the FE mesh and specifically on the size of the finite elements. The model illustrated in Fig. 2 has been discretized with a triangular mesh and the element size has been set to 1/10 of the shortest wavelength to be analysed, according to [22] and [23], where it is recommended to have at least 10 nodes per wavelength. The mesh was refined in the proximity of the solid/air transition regions and in correspondence with the heat source generated by the laser pulse.

An implicit analysis with a generalised-a (alpha) time dependent-solver was implemented.

2.2. The tested wheelset

The 2D numerical model, described in Section 2.2, was developed to drive the testing of the experimental LUT on the train wheelset provided by Trenitalia (see Fig. 5) in whose axle two standard fatigue cracks, [4], were simulated:

- Defect A located on the axle surface at 16 mm from the fretting region between the axle and the wheel,
- Defect B located on the fitting region.

Defects geometrical characteristics are reported in Fig. 6. Those defects were simulated in the 2D numerical model in order to determine their effect on the ultrasound signal received by the LUT air-coupled probe.

(a) (b)

Fig. 5. Trenitalia train wheelset - zoom of the defected area (a) and wheelset (b).

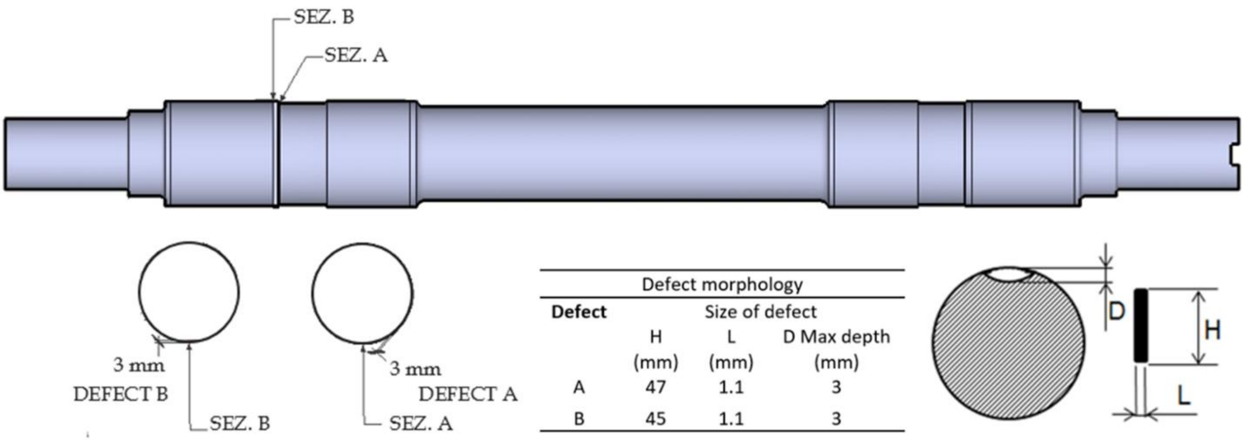

Fig. 6. Defects simulated in the wheelset.

3. Numerical results

The propagation of the elastic waves within the undamaged 2D wheelset section and in the air domain at different time intervals is shown in Fig. 7. The red dashed arrow indicates the laser source position, from which the elastic waves are generated. Observing the propagation pattern at 15 μs (Fig. 7 (b)), the different modes of propagation can be evidenced:

- the longitudinal (L) and shear (S) waves that propagate towards the inside of the train axle,

- the superficial waves, that can be distinguished into Rayleigh waves (R) and surface skimming bulk waves (S_k) (longitudinal S_L – shear S_S). The S_L and S_S waves mark the intersection with the surface of the longitudinal and shear wave fronts, respectively, which originate from the bulk source [17].

The bulk and Rayleigh waves can be distinguished by considering their propagation velocity in the solid material (i.e. steel) which are 5650m/s (for the SL wave), 3100m/s (for the SS wave) and 2905m/s (for the R wave), [19]. Those values are in good agreement with the measured ones in the axle material as reported in [10]. At the time instant of 15 μs the SL wave front will be at 85 mm from the laser source, the SS one at 47 mm and the R one at 44 mm. Those data allow to position the different waves in the plot of Fig. 7(b). In order to better evidence the propagation direction of the different modes Fig. 8 reports arrow plots filtered at the spatial position of the R, SS and SL waves.

The directivity pattern of the longitudinal wave that propagate in the air domain originated from the elastic waves travelling along the wheelset section can be plotted in polar coordinates, as in Fig. 7(e). This plot is useful to identify the optimal orientation of the receiver probe in order to catch the maximum level of the signal. The plot indicates that the maximum efficiency in the propagation will occur at an angle of 33 deg with respect to the axle surface normal.

Fig. 9 and Fig. 10 reports the same propagation pattern and directivity plot but for the case of damaged axle and specifically with the defect A and B respectively. It is noticeable that when the Rayleigh wave encounters the defect it is reflected: the reflected wave is marked as R_R in Fig. 9(b) and Fig. 10(b). The directivity plots evidences that it occurs an attenuation of about 80% for the defect A and 70% for the defect B of the propagating waves associated to the defect presence either in the solid either in the air domain.

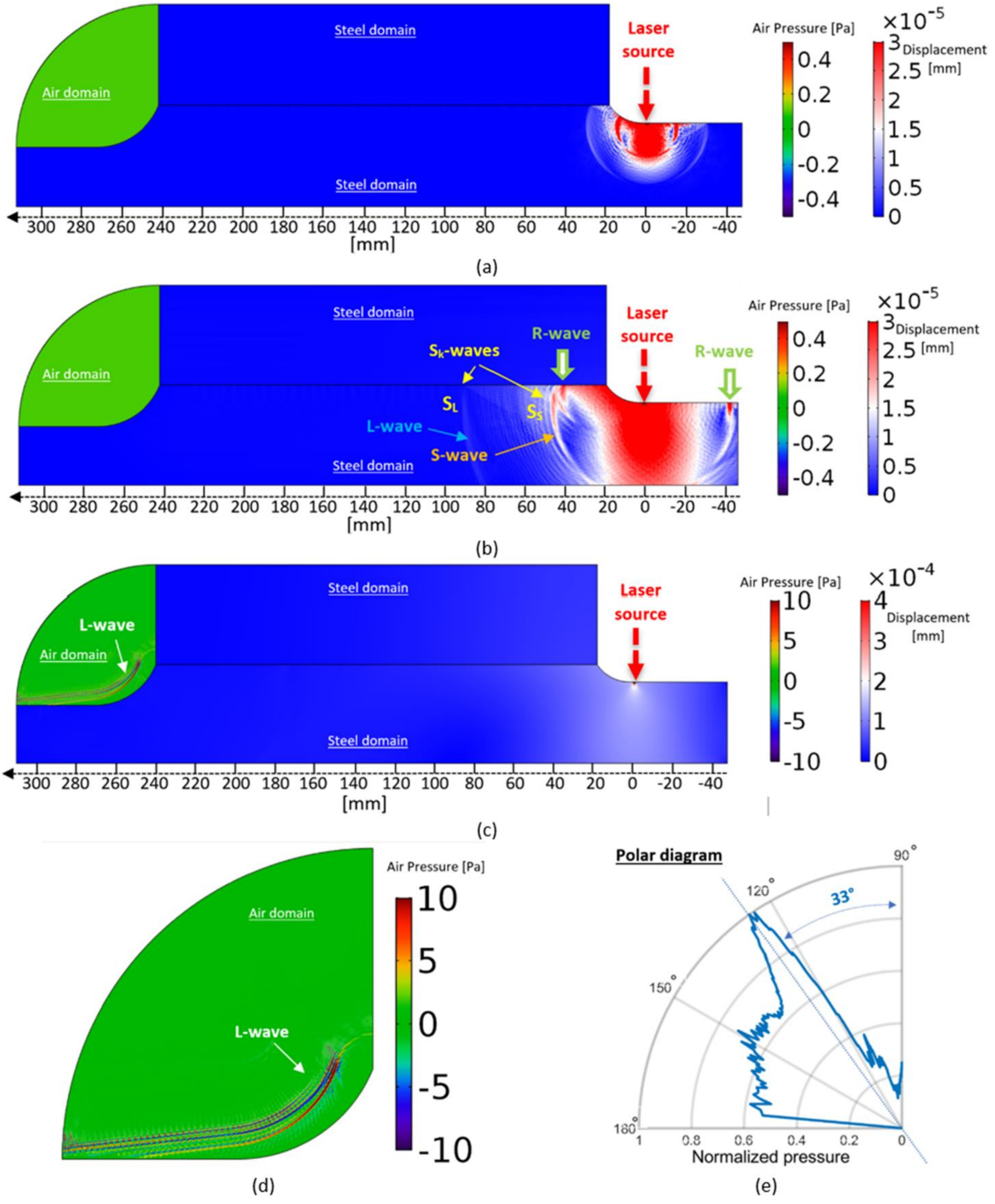

Fig. 7. Propagation of the elastic waves in the undamaged 2D wheelset section at different time instants: 5µs (a), 15 µs (b), 110 µs (c); propagation of the elastic waves in the air domain (d); directivity plot in the air domain (e).

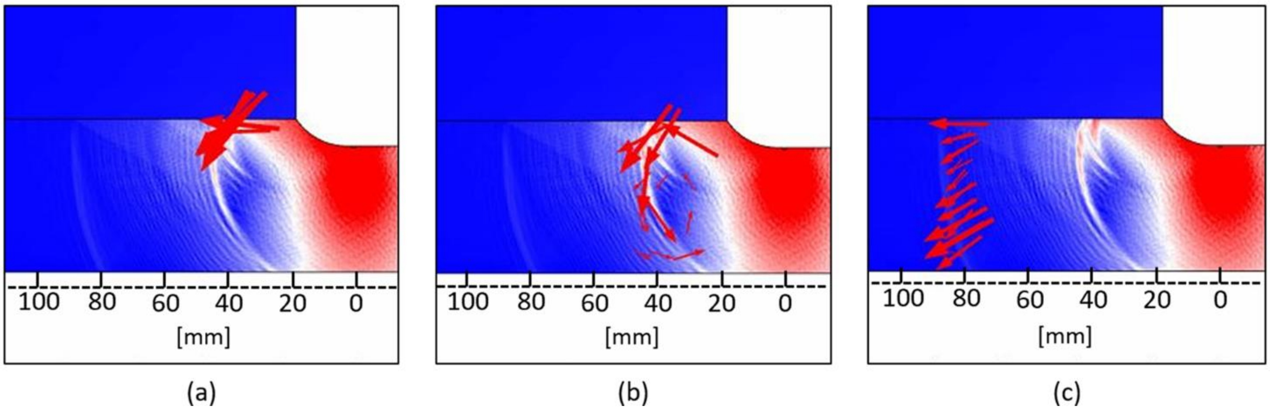

Fig. 8. Propagation direction of the elastic waves R (a), SS (b), SL (c) at the time instant of 15 μs.

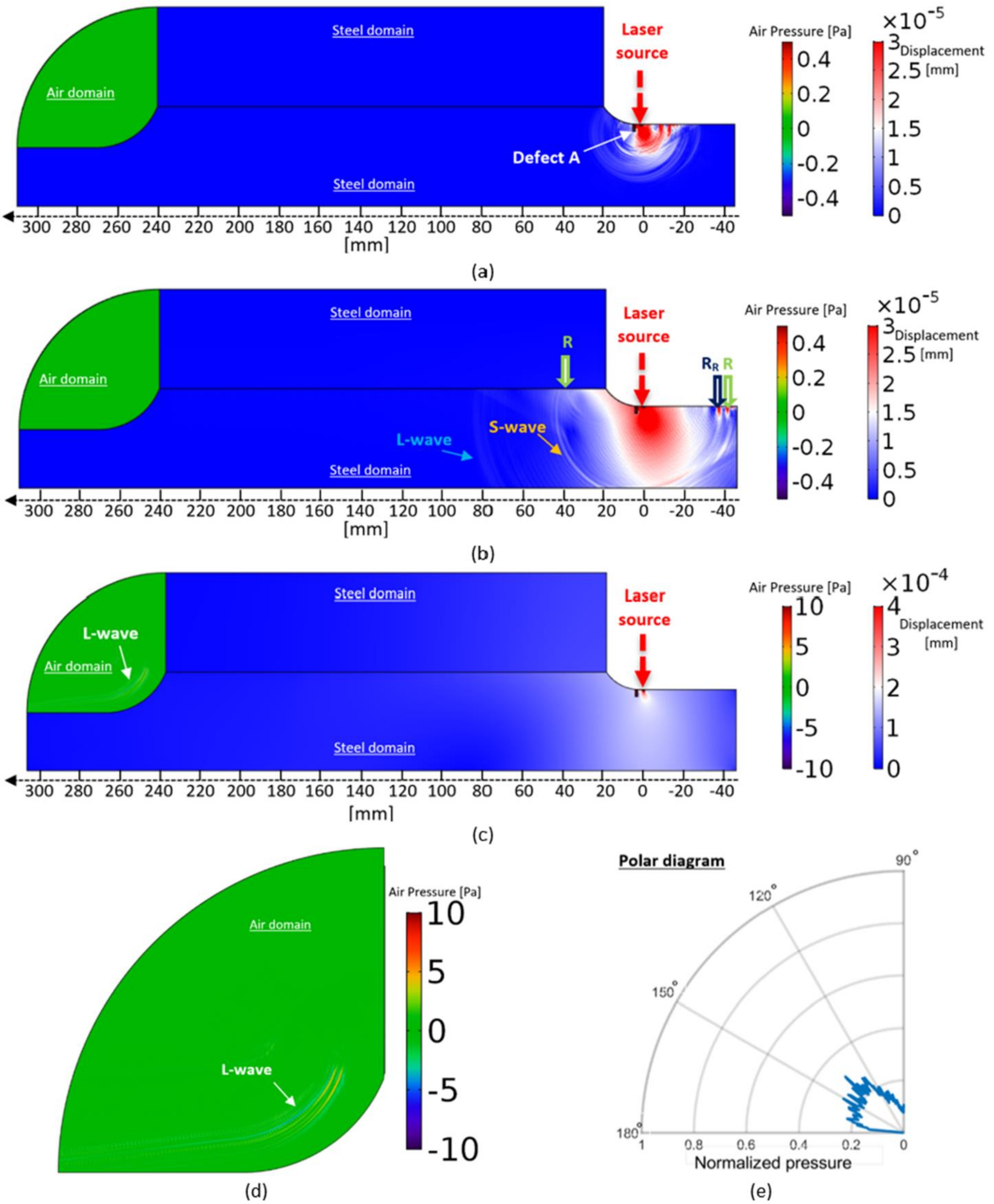

Fig. 9. Propagation of the elastic waves in the 2D wheelset section with defect A at different time instants: 5µs (a), 15 µs (b), 110 µs (c); propagation of the elastic waves in the air domain (d); directivity plot in the air domain (e).

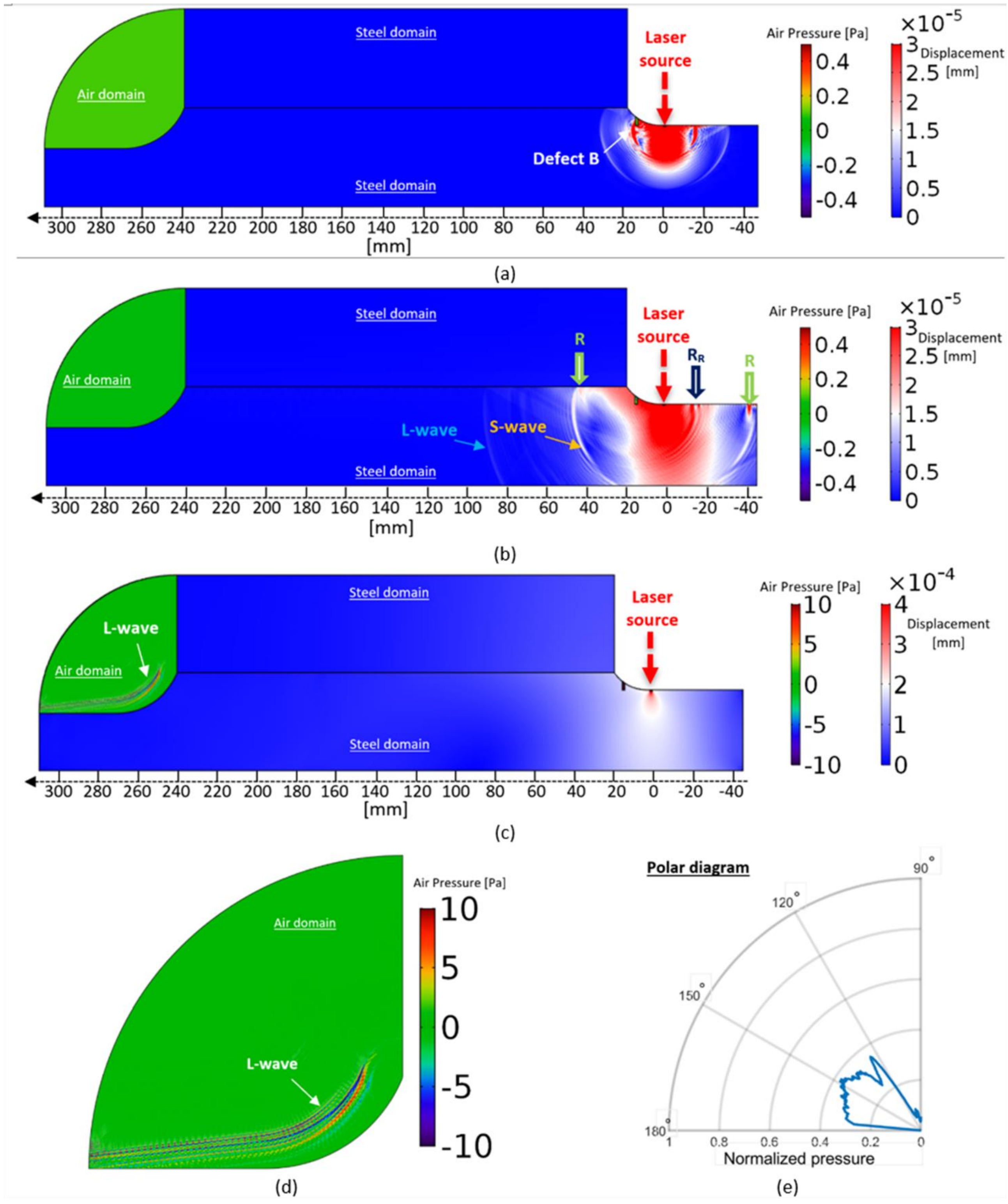

Fig. 10. Propagation of the elastic waves in the 2D wheelset section with the defect B at different time instants: 5μs (a), 15 μs (b), 110 μs (c); propagation of the elastic waves in the air domain (d), directivity plot in the air domain (e).

The 2D numerical model in the Fig. 11(a), allows to analyse the ultrasound signals (Fig. 11(b)) that will be acquired during the experimental tests by a non-contact receiving transducer placed on the opposite side of the press fitting area (point P in Fig. 11(a)) with respect to the pulsed laser impinging point (red dashed arrow in Fig. 11(a)).

The distance between the laser impinging position and the detection one was set to 257.5 mm that corresponds to a distance of about 252 mm along the axle profile and 5.5 mm in the air along the y' axis which corresponds to the direction of maximum efficiency. 5.5 mm is the minimum distance in air required considering the encumbrance of the receiving probe (active diameter of 19 mm, probe diameter of 33 mm and inclination of 33 deg) used in the experimental tests.

The three waveforms calculated at point P in Fig. 11b were obtained by running the model with and without defects and the waveforms were filtered in the frequency range of the ultrasound probe used in the experiments (500 kHz ± 100 kHz), to evidence only the frequency content that will be measured in the actual test. The waveforms have been plotted with normalized amplitude. By observing the waveforms, it is clear that the bulk elastic waves (L and S) do not propagate up to the probe position. Their efficiency in the air domain is weak and therefore they are not sensed by the probe [18]. Only the surface waves (R, and SL, SS) propagates through the air domain and are visible in the time histories of Fig. 11(b). Their occurrence in time has been identified by knowing their propagation velocity as explained in the description of Fig. 7.

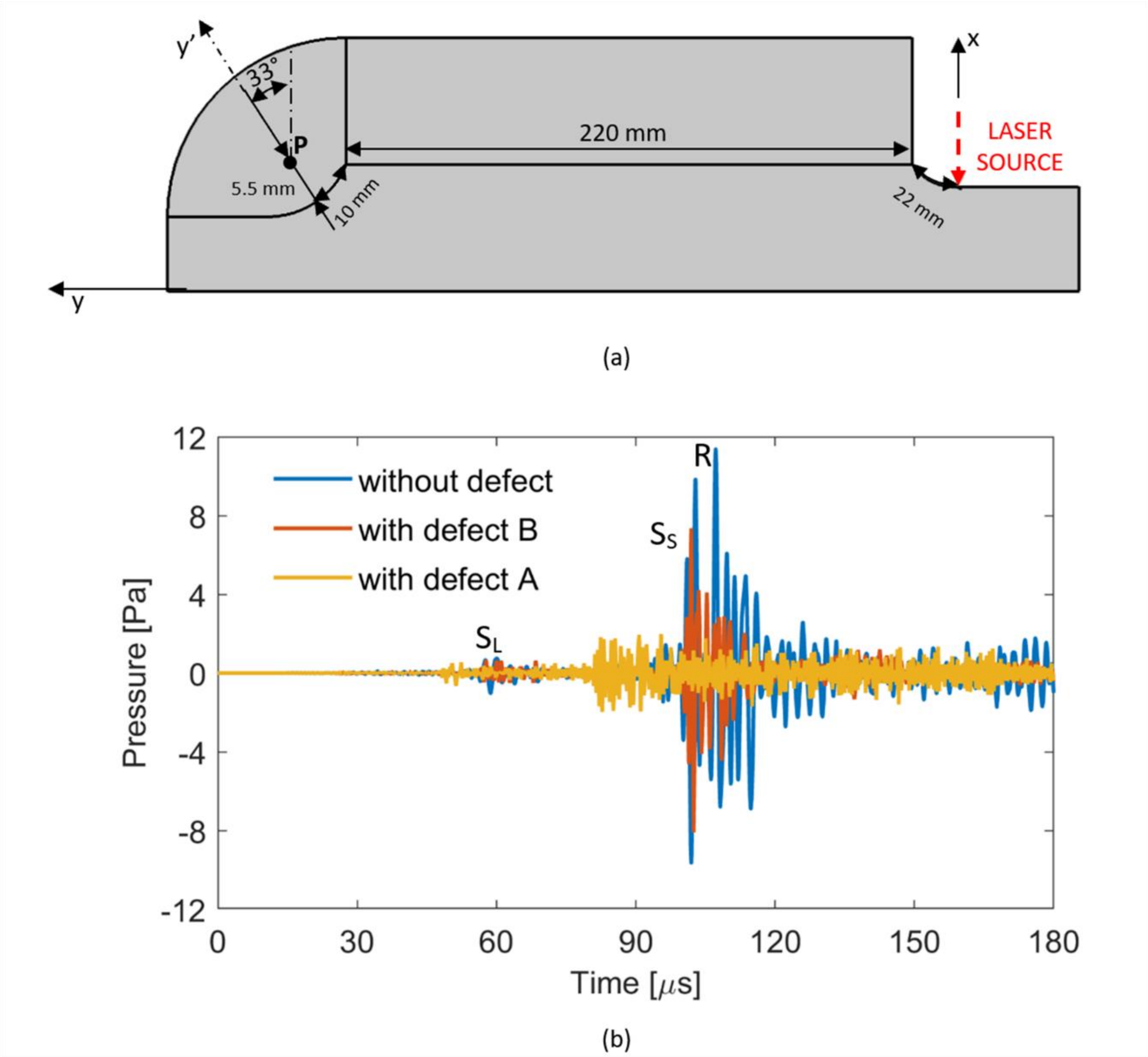

Fig. 11. Position of the probe where the pressure waveform signals have been exported, point P (a) and plot of those pressure waves in the case of undamaged axle and axle presenting a defect type A or a defect type B (b).

The time histories plotted in Fig. 11(b) are coherent with that deduced from the directivity plots, i.e. the presence of the defect strongly attenuates the elastic waves propagation.

In order to identify the presence of the defect from the time histories acquired, a damage indicator has been assumed and specifically the RMS (Root Mean Square) contrast defined as the ratio between the RMS calculated from the time history measured on a damaged area and the one measured on a sound region:

$$RMS_{contrast} = 20log\frac{RMS_{damaged\ area}}{RMS_{undamaged\ area}} \quad (2)$$

By observing the time histories, it can be evidenced that the defect A attenuates all the surface waves, both the skimmed and the Rayleigh, while the defect B attenuates only the Rayleigh wave. With the aim to identify the defect type it is possible to select the time window within the signal to consider only the portion which is effectively sensitive to the presence of the defect. For instance, for the defect A, the time window can be centred around the time of arrival of both the SS and Rayleigh wave, while for the defect B, it must be cantered only around the time of arrival of the wave R. To evaluate the centre of the window and its length, the RMS contrast has been calculated by analysing the time history with sliding windows centred at time steps from 40 μs to 140 μs with an increment of 1 μs and length from 5 to 60 μs. The plot of the RMS contrast for the different time windows is reported in Fig. 12 for both defect A and B. In these plots, it is evidenced the position of the RMS contrast minimum (black dot) which indicates that for the defect A the time window containing the most sensitive signal to the presence of the defect is centred at 98 μs and has a length of 5 μs. For the defect B the time window is centred at 115 μs and has a length of 12 μs. Those data will be used to analyse the time histories acquired in the experimental campaign.

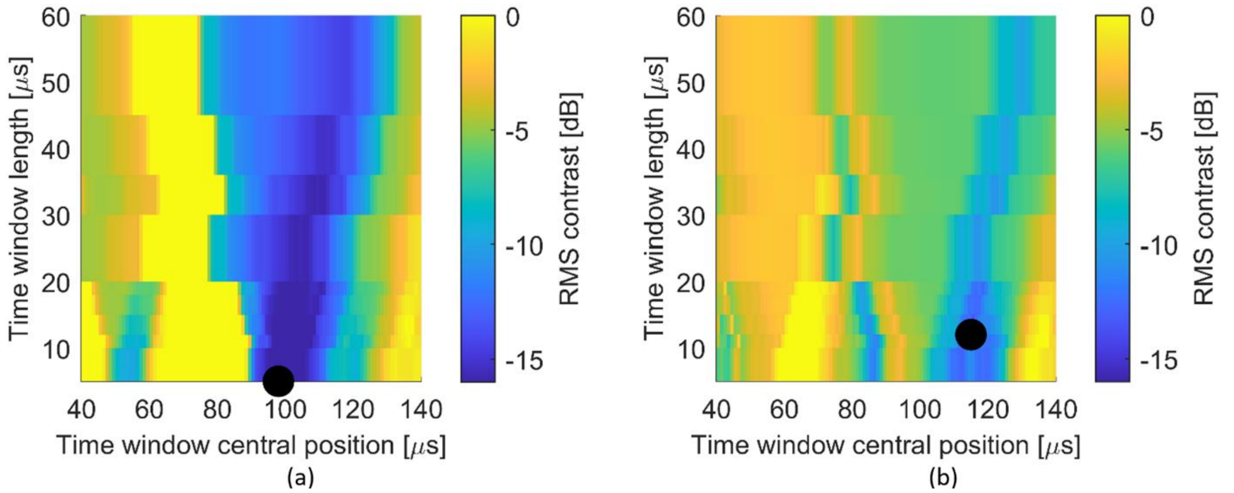

Fig. 12. Surface wave sensitivity analysis in the presence of defects A (a) and B (b); RMS contrast at several time windows.

4. Experimental set-up

The wheelset was mounted on a support that made it possible to control its rotation, so as to be able to scan the axle surface along a circumference. The probes were installed on a frame where they could move along the tangential direction. Therefore, the complete tangential surface of the axle could be inspected by the laser-ultrasonic system, see Fig. 13.

The laser-ultrasonic system was made up of a pulsed laser source and an air-coupled ultrasound piezoelectric probe. The laser source was a Nd:YAG IR laser (1064 nm) with 82 mJ energy able to generate laser pulses of 12 ns duration. The laser wavelength was chosen as a compromise between the energy, the pulse duration [25] and the penetration depth [18]. The ultrasound probe was an Ultran Group NCG 500 with 19 mm diameter of active area and 500 kHz of operating frequency. The probe orientation was set according to the FE model results (see Fig. 11), i.e. it was inclined with respect to the normal to the axle surface of 33 deg. The ultrasound probe conditioning system was a JSR Ultrasonics DPR 300 Pulser/Receiver. The ultrasound signals were amplified with a gain level of 69 dB and acquired with a high-speed digitizer board NI PXI-5122 (100 MHz bandwidth). The laser beam was guided towards the axle under test by means of an arm connected to the pulsed laser cavity as shown in Fig. 13.

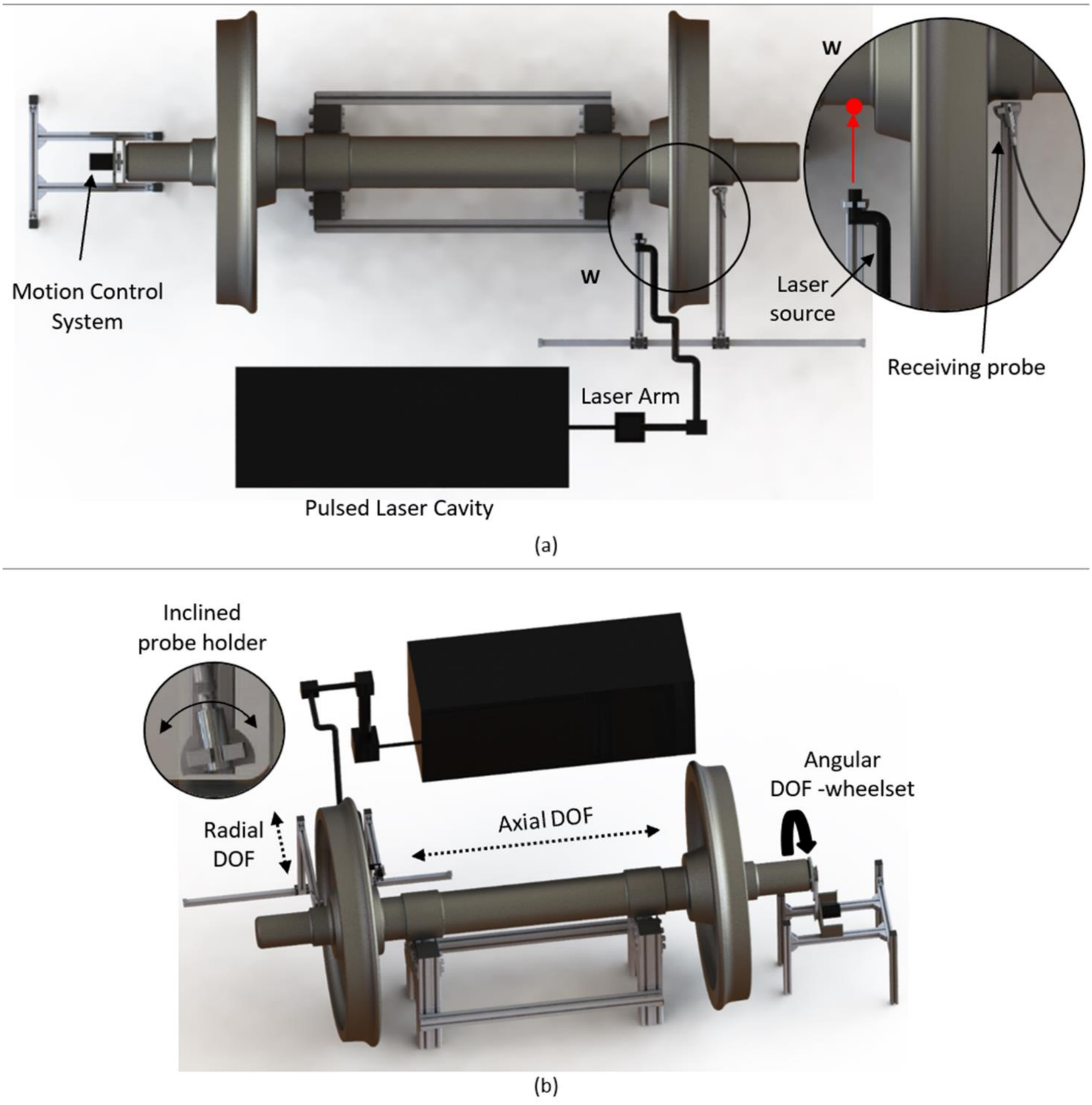

Fig. 13. Configuration of the laser-ultrasonic scanning system-test bench setup (a) and the DOF scanning system (b).

The close-up reported in Fig. 13 and named section W shows the laser source and the receiving probe installed on opposite sides of the wheel. This configuration allowed to detect defects occurring between the source and the receiving probe even if they were located in the shrinking region. A collimated laser beam with a diameter of 6 mm was used to keep the generation of ultrasonic waves within a thermo-elastic regime [24]. The probe was handled by a positioning system that allowed to move the probe in radial and axial direction with respect to the axle, as shown in Fig. 10 by the radial and axial DOF

(Degree Of Freedom). The angular DOF was controlled by an electric motor that let the axle to rotate about its axis. The rotation angle was measured by an integrated encoder. The angular position of the defects A and B with respect to the laser source/receiving probe is illustrated in Fig. 14. At reference position (0 degree rotation of the axle), defect A is located between angle 20 deg and angle 50 deg while defect B is located between angle 110 deg and 138 deg. The angular position considered in Fig. 16 refers to the configuration reported in Fig. 14. The axle sector considered in the discussion of results is of 160 deg as sketched in Fig. 14.

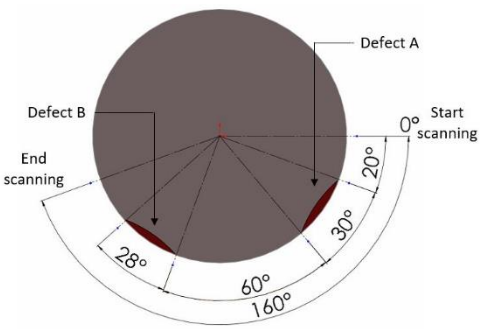

Fig. 14. Angular position of the defect A and B with respect to the reference angle of 0 deg.

5. Experimental results and correlation with numerical data

The experimental set-up (i.e. laser and probe positions), the axle section tested and the defect location are shown in the subplot (a) of Fig. 15 and Fig. 16 for defect A and B respectively. The angular position of the receiving probe and its distance from the axle is described in section W. The laser source and the generation path of the ultrasound waves produced by the impact of the laser pulse onto the axle surface are sketched in section Z.

For each configuration, a series of ultrasound time histories with a duration of 100 µs starting from 40 µs with respect to the trigger associated to the laser pulse were acquired at every scanning position along the arc considered. A comparison between the time histories measured and simulated at two angular positions located within and outside the damaged region is reported in Fig. 15 (b) and Fig. 15 (c), respectively, for the defect A, and in Fig. 16(b) and Fig. 16(c), for the defect B. Obviously, also in the experimental case, the attenuation due to the presence of the defect is evident as it arose for the numerical data. That attenuation is clear also from the conventional B-scan plots reported in Fig. 17(a) and (b) for the two defects. It should be pointed out, that if the defect is sub superficial or located on the back of the sample, bulk waves will be sensitive to the presence of the defect rather than the Rayleigh ones. In this case the effect on the received signal will be an increase in the amplitude of the signal due to the received echo.

If the attenuation is calculated using the damage indicator described in Section 3, equation (2), i.e. the RMS contrast, by applying the procedure explained in the same section for the numerical data, the plots reported in Fig. 16(c) and (d) are attained. Spherically, those plots have been obtained by using a time window of 5 μs and 12 μs for defect A and B respectively. For the binarization of those plots a threshold of 6 dB has been applied, according to [26].

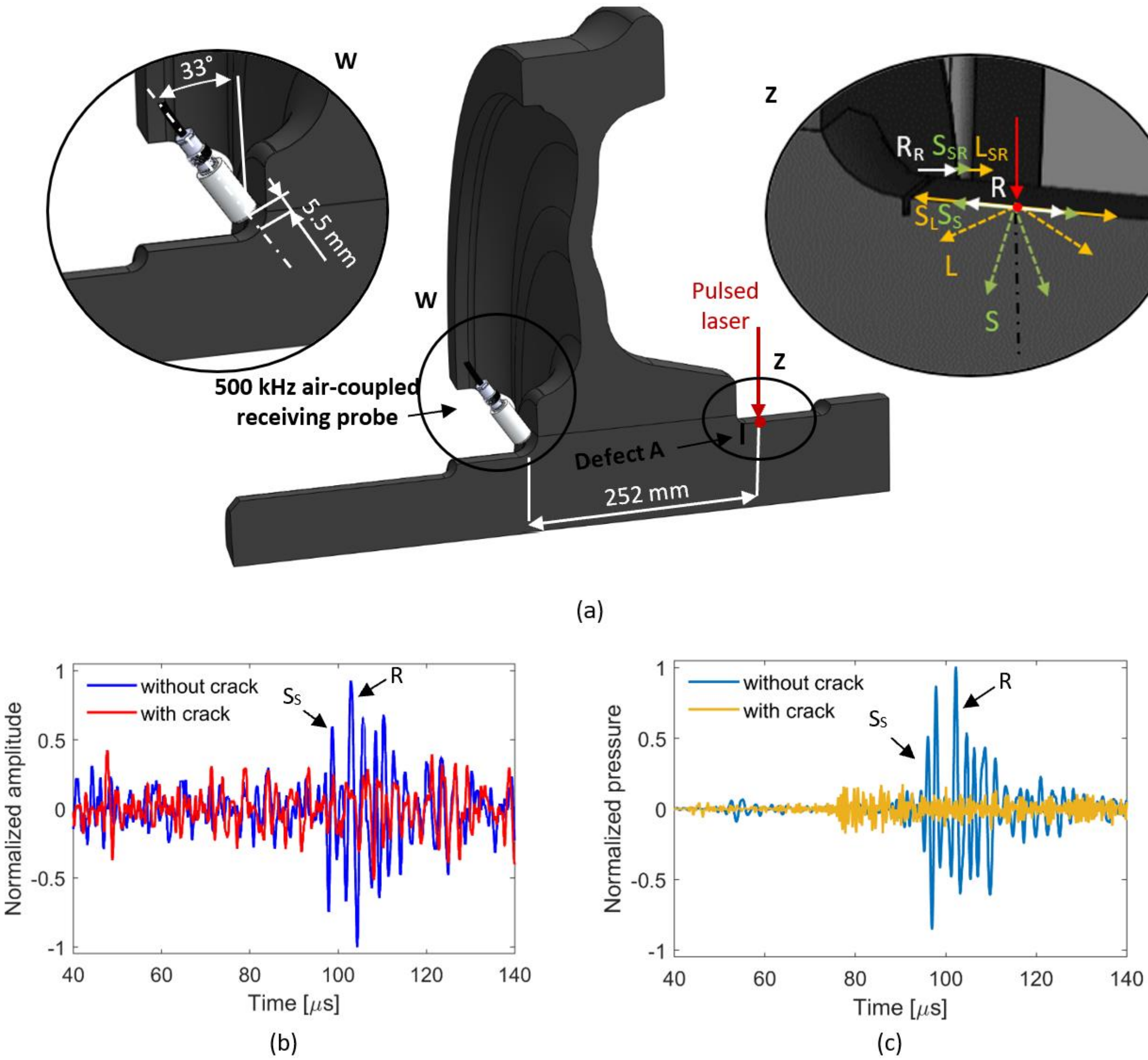

Fig. 15. Numerical-experimental data comparison for axle presenting a type A defect, experimental set-up (a), experimental data: close up of the time histories around the superficial waves - case of damaged and undamaged axle (b) and numerical data: close up of the time histories around the superficial waves - case of damaged and undamaged axle (c).

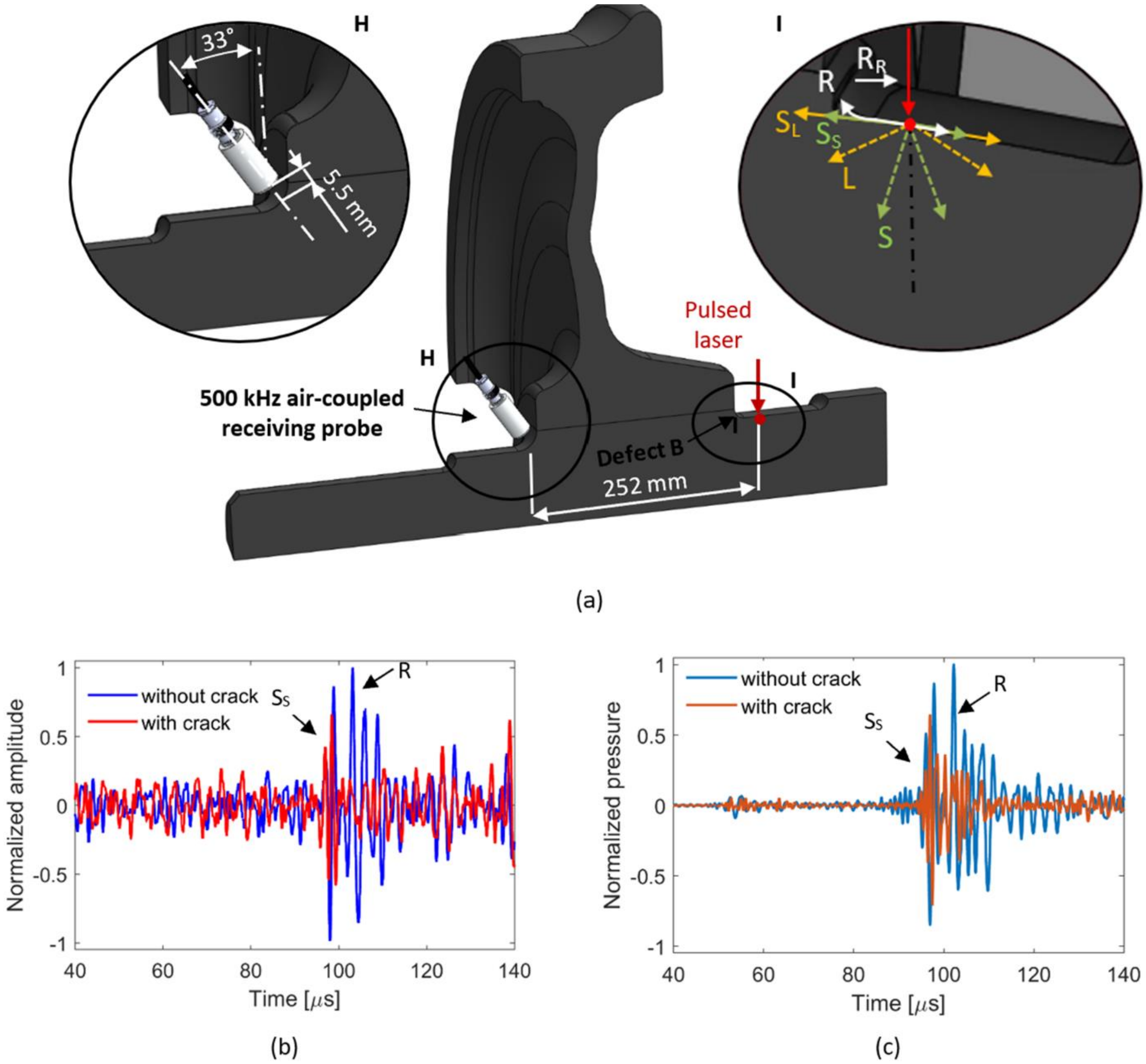

Fig. 16**.** Numerical-experimental data comparison for axle presenting a type B defect, experimental set-up (a), experimental data: close up of the time histories around the superficial waves - case of damaged and undamaged axle (b) and numerical data: close up of the time histories around the superficial waves - case of damaged and undamaged axle (c).

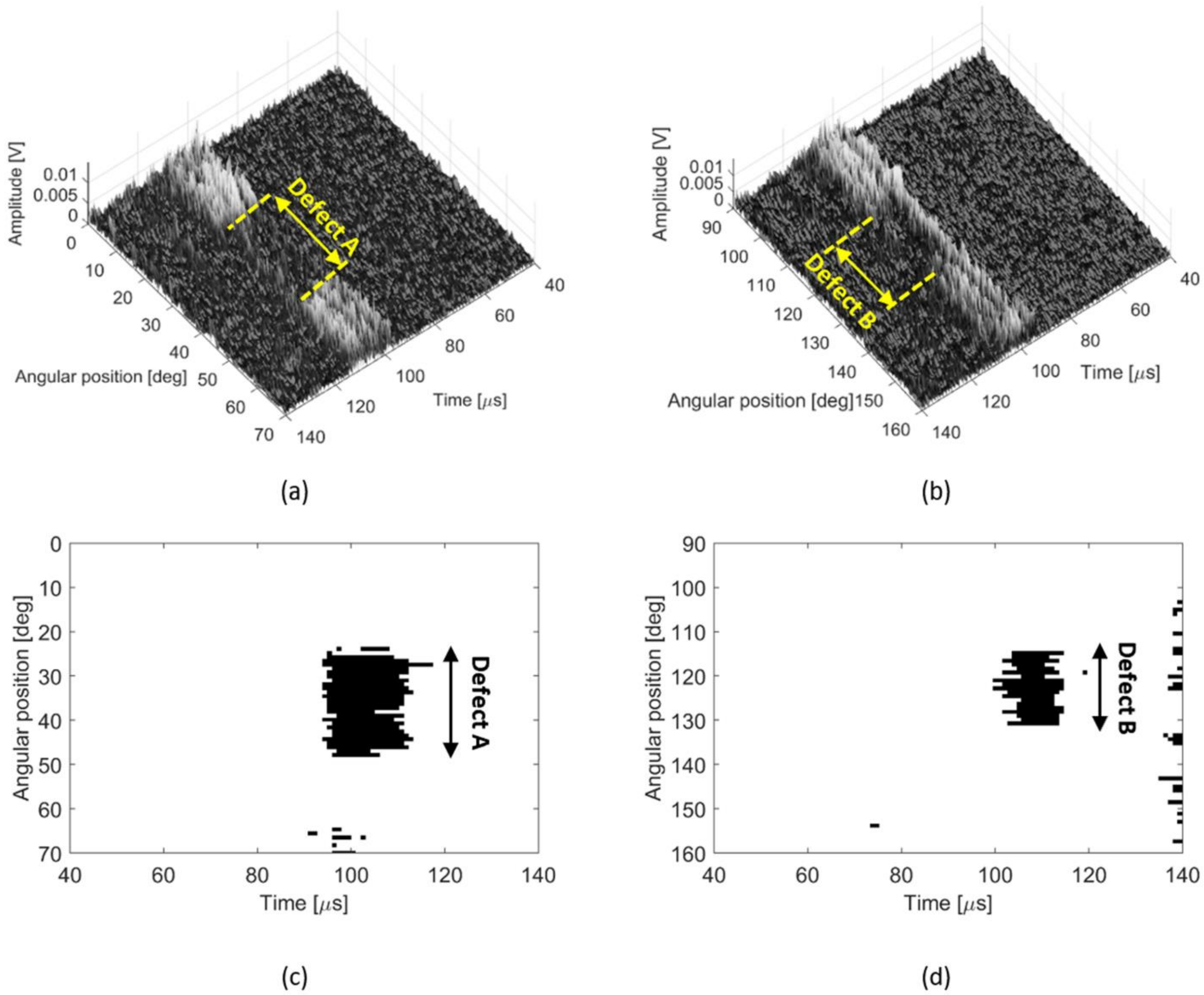

Fig. 17. B-scan plots for defect A (a) and defect B (b) and binary RMS contrast plots for defect A (c) and defect B (d)

6. Conclusions

The paper has shown a dedicated FE numerical model to optimize the experimental non-contact LUT measurement procedure. This is the first main innovation of the paper since for the first time a complete FE model has been implemented considering the propagation of ultrasound waves into both solid and air domain.

The results of the FE model were fundamental as a guide for the experiment since they allowed to determine a priori the energy of the laser source which allows to limit the generation of the ultrasound wave within the thermoelastic-ablative limit. This is the second main innovation of the paper which demonstrated the possibility of working in the thermoelastic regime maintaining an adequate level of accuracy for defect diagnostics. The FE model results have been used also to estimate the angular position of the receiving probe, the propagation mode of the ultrasonic wave most sensitive to the presence of the defect and therefore the time window to observe within the acquired time history. It has been evidenced by the numerical model and demonstrated by the experiments that a defect close to the fretting area (as the defect B) attenuates only the Rayleigh wave and not the skimmed ones while a defect located on the fillet attenuates both the propagation modes (as the defect A). The time windows to be analyzed are therefore different and the numerical model indicated that the best window lengths is 5 μs for the defect A and 12 μs for the defect B.

It is clear that the combination of numerical and experimental results with respect to the traditional purely experimental approach has allowed for greater flexibility and gave the opportunity to optimize the control procedure using the LUT technique with significant savings in terms of time spent for experimental design and test realization.

REFERENCES

[1] R. Hannemann, P. Köster, M. Sander, Fatigue crack growth in wheelset axles under bending and torsional loading, International Journal of Fatigue 118 (2019) 262-270.

[2] V. Grubisic and G. Fischer, Railway axle failures and durability validation, Proceedings of IMechE Part F: J Rail and Rapid Transit (2012) 226(5) 518–529.

[3] S. Foletti, S. Beretta, F. Bertozzi, M. Carboni, S. Cervello, D. Regazzi, Experiments on crack propagation and threshold at defects in press-fits of railway axles, Procedia Structural Integrity 7 (2017) 484-491.

[4] Railway applications – In-service wheelset operation requirements – In-service and off-vehicle wheelset maintenance, in EN 15313:2016.

[5] A. Rohrschneider, H. hintze, Thomas oelschlägel, Further development of the ultrasonic testing of hollow axles, 11th European Conference on Non-Destructive Testing (ECNDT 2014), October 6-10, 2014, Prague, Czech Republic.

[6] M. Carboni, S. Cantini, C. Gilardoni, Validation of the Rotating UT Probe for InService Inspections of Freight Solid Axles by Means of the MAPOD Approach, 5th European-American Workshop on Reliability of NDE, Germany – October 7-10, 2013.

[7] J. Peng, X. Gao, Y. Zhang, Z. Wang, C. Peng, Y. Tan, K. Yang, B. Zhao, An ultrasonic technology study for subsurface defect in railway wheel tread, in: Proceedings of 11th European Conference on Non-Destructive Testing (ECNDT), Prague, Czech Republic, 2014.

[8] N. Montinaro, G. Epasto, D. Cerniglia, E. Guglielmino, Laser ultrasonics for defect evaluation on coated railway axles, (2020) NDT and E International, 116, DOI: 10.1016/j.ndteint.2020.102321.

[9] N. Montinaro, G. Epasto, D. Cerniglia, E. Guglielmino, Laser Ultrasonics Inspection for Defect Evaluation on Train Wheel, NDT & E International, (2019) 107:102145.

[10] A. Cavuto, M. Martarelli, G. Pandarese, G.M. Revel, E.P. Tomasini, Experimental investigation by laser ultrasonics for high speed train axle diagnostics, Ultrasonics 55 (2015) 48–57.

[11] S. Kenderian, B. B. Djordjevic, D. Cerniglia, Laser-air, hybrid, ultrasonic testing of railroad wheels, patent n. US 6,862,936 B2, Mar. 8, 2005.

[12] A.Cavuto, M. Martarelli, G. Pandarese, G.M. Revel, E.P. Tomasini, Train wheel diagnostics by laser ultrasonics, Measurement, Volume 80, February 2016, Pages 99-107, ISSN 0263-2241, http://dx.doi.org/10.1016/j.measurement.2015.11.014.

[13] A. Cavuto, M. Martarelli, G. Pandarese, G.M. Revel, E.P. Tomasini, Experimental investigation by Laser Ultrasonics for train wheelset flaw detection, 2018, Journal of Physics: Conference Series, 1149 (1), DOI: 10.1088/1742-6596/1149/1/012015.

[14] A. Mineo, D. Cerniglia, A. Pantano, Numerical study for a new methodology of flaws detection in train axles, Ultrasonics (2013), http://dx.doi.org/10.1016/j.ultras.2013.10.008.

[15] M. Madia, S. Beretta, U. Zerbst, An investigation on the influence of rotary bending and press fitting on stress intensity factors and fatigue crack growth in railway axles, Engineering Fracture Mechanics 75 (2008) 1906–1920.

[16] A. Cavuto, F. Sopranzetti, M. Martarelli, G.M. Revel, Laser-ultrasonics wave generation and propagation FE model in metallic materials, in: Proceeding of COMSOL Conference, Rotterdam, 2013.

[17] J. Wanga, Z. Shen, B. Xu, X. Ni, J. Guan, J. Lu, Numerical simulation of laser-generated ultrasound in non-metallic material by the finite element method, Optics & Laser Technology 39 (2007) 806–813.

[18] C.B. Scruby, L.E. Drain, Laser Ultrasonics: Techniques and Applications, CRC Press, 1990.

[19] JL. Rose, Ultrasonic waves in solid media. Cambridge, UK: Cambridge University Press; 1999, ISBN: 0521640431B.Q. Xu, Z.H. Shen, X.W. Ni, J. Lu, Thermal and mechanical finite element modeling of laser-generated ultrasound in coating-substrate system. Optics Laser Technol 2006;38(3):138–145.

[20] M.S. Malik, A. Cavuto, M. Martarelli, G. Pandarese, G.M. Revel, Reliability Analysis of Laser Ultrasonics for Train Axle Diagnostics based on Model Assisted POD Curves, AIP Conference Proceedings 1600, 396 (2014); https://doi.org/10.1063/1.4879608.

[21] M.C. Bhardwaj, High transduction piezoelectric transducers and introduction of non-Contact analysis, NDT.net - January 2000, Vol. 5 No. 01.

[22] D. Cerniglia, A. Pantano, C. Mineo, Influence of laser beam profile on the generation of ultrasonic waves, Appl. Phys. A. 105 (2011) 959–967.

[23] D. Alleyne, P. Cawley, A two-dimensional Fourier transform method for measurement of propagating multimode signals. Journal of the Acoustical Society of America 89 (3) (1991) 1159–68.

[24] P. Castellini, G.M. Revel, L. Scalise, R.M. De Andrade, Experimental and numerical investigation on structural effects of laser pulses for modal parameter measurement, Opt. Lasers Eng. 32 (6) (2000) 565–581.

[25] S. J. Davies, C. Edward, G. S. Taylor and S B Palmer, Laser-generated ultrasound: its properties, mechanisms and multifarious applications J. Phys. D Appl. Phys. 26 (1993) S29-348.

[26] Standard, UNI-EN ISO 16827:2014, Non-destructive testing – ultrasonic testing –characterization and sizing of discontinuities; 2014.